Additive Manufacturing 35 (2020) 101216

Contents lists available at ScienceDirect

Additive Manufacturing

journal homepage: www.elsevier.com/locate/addma

Research Paper

Powder Reuse in Electron Beam Melting Additive Manufacturing of Ti6Al4V: Particle Microstructure, Oxygen Content and Mechanical Properties

A. Montelione[a], S. Ghods[a], R. Schur[a], C. Wisdom[a], D. Arola[a,b], M. Ramulu[b,*]

[a] Department of Materials Science and Engineering, University of Washington, Seattle, WA, USA
[b] Department of Mechanical Engineering, University of Washington Seattle, WA, USA

ARTICLE INFO

Keywords:
Additive manufacturing
Titanium
Electron beam
Powder bed fusion
Powder reuse
Nanoindentation
Microstructure
Oxygen content

ABSTRACT

As metal Additive Manufacturing (AM) becomes more widely adopted in the aerospace and orthopedic industries, there is increasing demand to improve part quality and reduce overall cost. The high cost of powder feedstock has raised interest in recovering unmelted powder in the build chamber and its reuse in subsequent builds. While degradation in powder properties with recovery and reuse can cause degradation in part properties, this topic has received rather limited attention. In this study the properties of Ti6Al4V metal powder are evaluated over 30 build cycles in Electron Beam Melting (EBM) AM. The morphological, microstructural, mechanical, and chemical changes are evaluated in cross-sectioned powder particles and compared to isolated control samples to understand the mechanisms of degradation. Results show that in response to the elevated build chamber temperature, the powder undergoes a sub-beta-transus aging heat treatment with powder reuse. Based on nanoindentation hardness measurements, the particles undergo an increase in near-surface hardness (up to 2 GPa) with respect to the core. Moreover, tint etching revealed an oxidized surface layers consistent with alpha case formation. The particle hardening appears to result from oxygen diffusion during powder recovery and not work hardening related to the mechanical aspects of that process. These results demonstrate the importance of managing/mitigating oxidation of metal powder feedstock to improve its reusability and increasing its overall lifetime.

1. Introduction

Metal powder bed Additive Manufacturing (AM) processes have become increasingly viable for applications in the aerospace and medical industries [1,2]. Electron Beam Melting (EBM) Powder Bed Fusion (PBF) is one of the most prominent methods for metal AM. This process uses an electron beam as the heat source to selectively melt and fuse metal powder layer-by-layer in the process of achieving the desired 3D geometry [3].

In EBM AM the printed parts are supported in a bed of powder, which reduces the need for extensive support structures that are characteristic of deposition processes [3]. However, the powder bed volume increases the quantity of powder feedstock needed to complete the build process, regardless of the part volume. Only a fraction of the powder in the build chamber is melted and utilized in the part. The remaining/surrounding powder is available for reuse after completion of the build and its recovery.

As a consequence of the relatively high cost of feedstock material, powder reuse is now considered an essential part of PBF processes and critical to maximizing the affordability of the process [4–6]. Indeed, a number of studies have been reported on various aspects of metal powder reuse in AM. Overall, prior investigations on reuse have distinguished that the powder quality can undergo changes with reuse that manifest through degradation in the mechanical properties of the metal [5–8]. Thus, powder reuse poses an important trade-off between process economics and part performance concerns.

Due to a combination of their excellent strength to weight ratios, biocompatibility and corrosion resistance, titanium alloys are used extensively in aerospace and medical applications [1,9–12]. Titanium alloys are also a major focus in metal AM via EBM [11,13,14] and Selective Laser Melting (SLM) [11,13,15]. The chemical resistance of titanium comes from its reactivity with oxygen. It forms an impervious surface oxide layer spontaneously in the presence of oxygen that prevents the underlying metal from reacting with the surrounding environment [16]. At high temperatures, however, the oxygen can diffuse into the metal to form an interstitially hardened layer known as alpha-

* Corresponding author at: Department of Mechanical Engineering, University of Washington, Mechanical Engineering Bldg, MEB 320, Box 352600, Seattle, WA 98195-2120, USA.
E-mail address: ramulum@uw.edu (M. Ramulu).

https://doi.org/10.1016/j.addma.2020.101216
Received 16 December 2019; Received in revised form 9 March 2020; Accepted 4 April 2020
Available online 07 May 2020
2214-8604/

case (α-case) [12,17–19]. Oxygen atoms occupy the interstitial sites in the HCP lattice, thereby causing a slight tetragonal lattice distortion that stabilizes the alpha phase and impedes dislocation motion through the lattice [17,20]. The near-surface case layer is harder than the underlying metal. It is also more brittle, and often undergoes microcracking, which can degrade the corrosion and fatigue resistance of the metal [18,19]. An increase in oxidation of the powder may foster an increase in oxygen content of the printed metal and contribute to the degradation of the mechanical properties seen in components built with reused powder [4–8,21,22,24]. This raises a concern in AM processes involving titanium and other anodic alloys that have tendency to react with oxygen. Indeed, PBF systems for metal AM are operated in inert environments to protect the molten metal from oxygen, either under argon atmosphere for SLM or under vacuum for EBM systems.

The oxygen content of titanium powder in AM processes reportedly increases with its reuse [5,6,21], and can exceed the allowable concentration limits outlined by ASTM specifications for this EBM PBF process [23]. One approach to temper the rise in oxygen content is to simply mix the reused powder with fresh (virgin) powder after each build cycle. However, the rise in oxygen content depends on the exposure time of the powder to air, and the humidity of the environment [5], which complicates the determination of processing methods for the most efficient use of powder. Therefore, blind mixing to refresh powder is a potential solution without fundamental understanding. There are important engineering concerns related to the powder reuse beyond its exposure to elevated temperature, including the changes in particle microstructure, depth of oxidized layer, changes in mechanical properties, etc. To the authors' knowledge, a detailed investigation of powder degradation in metal PBF AM by EBM that addresses these concerns has not been reported.

The primary objective of this investigation is to evaluate the changes in properties of titanium powder with its reuse in EBM AM. The effort explores oxygen contamination of the powder with reuse over a large number of build cycles, and the primary contributing mechanisms, through a quantification of changes in the microstructure and mechanical properties of individual powder particles. Results of the various methods of quantification are discussed in detail and the implication to future powder reuse strategies are discussed.

2. Materials and Methods

2.1. Material

Fifty (50) kg of Grade 5 Titanium Alloy (Ti6Al4V) powder was purchased from the machine manufacturer (ARCAM: Batch P1303, Part #430944) for this study. The powder was used in sequential standardized builds performed using a commercial powder bed fusion system for EBM (ARCAM, Model A2X, Sweden). A total of thirty consecutive builds were performed, with the excess powder from each build being collected and reused in the subsequent build. A standardized build was performed in each cycle, which consisted of approximately 40 cm^3 of metal, including 0.6 cm^3 of support metal. The total volume of metal powder in the build chamber was 2966 cm^3, based on a total build height of 104 mm. The build chamber was preheated to 650 °C for each build, according to the default machine theme. The average build time for each cycle was approximately 16 hours, giving a total build time of approximately 480 hours for all 30 builds. More details are listed in Ghods et al., [22]. After each build, the partially sintered powder block was removed from the ARCAM machine and transferred to the powder recovery system (PRS). There, compressed air and loose titanium powder was used to free the encapsulated printed parts from the sintered powder block and loosen the remaining powder. This volume of processed powder was mixed with the powder remaining in the hoppers of the EBM machine, sieved (#125 mesh) to remove large particles, and returned to the machine for the next build cycle.

A separate batch of virgin powder was run continuously through the PRS system for 30 hours to simulate the effects of the repeated air blasting on an accelerated schedule. This powder underwent the mechanical deformation associated with the recovery process without the effects of the thermal variations associated with the build cycles. Samples of this powder were taken after every 10 hours of PRS treatment for analysis, and labeled t10, t20 and t30.

2.2. Alpha Case Standard

To validate the methods used to detect the presence of an alpha case in the samples, a lab standard was produced using available materials. A sample of virgin powder was subjected to a furnace heat treatment at 760 °C for 2 hours in ambient air, followed by air cooling. The conditions were selected based on a previous study reported by Pitt et al. [26] investigating alpha case development on titanium.

2.3. Sample Preparation

The powder samples were first mounted in Struers EpoFix two-part epoxy resin within a square plastic mold (approx. 1 cm x 1 cm) to establish a shape that helped to index and track individual powder particles. Individual particles are identified by their powder sample and an arbitrary particle number (e.g. b30p19 to distinguish particle 19 of build 30 powder). To aid in the impregnation of the powder samples with epoxy, they were placed in a vacuum chamber after adding the epoxy to the mold. After setting, the square powder mount samples were extracted from the plastic mold and then mounted in 30 mm cylindrical molds involving the aforementioned epoxy resin. Once cured, the powder samples were ground using silicon carbide papers with successively smaller particles to #800 grit. Polishing was then performed using 6 and 3 μm DiaLube diamond particle suspensions on an Allied High Tech White Label pad and a Struers MD-Dac pad, respectively. The final polish was achieved using a 0.05 μm colloidal silica attack polish solution containing 5% ammonium hydroxide and a small amount of hydrogen peroxide, on a Struers MD-Chem pad. The polished samples were etched, starting with Kroll's reagent (etchant #192 of ASTM E407-07 [25]) by partial immersion for 10 seconds, followed by an ammonium biflouride (ABF) tint etch (etchant #217 of ASTM E407-07 [25]). Fig. 1 shows an alpha case layer revealed by this tint etching process on a wrought bar of Ti6Al4V; the alpha case layer appears bright relative to the remainder. After optical analysis, the samples were repolished using the aforementioned methods to remove the etched topography and re-establish a smooth surface with mirror finish, as required for nanoindentation and SEM analysis.

2.4. Sample Analysis

2.4.1. Optical Microscopy

The powder samples were evaluated via optical microscopy using a

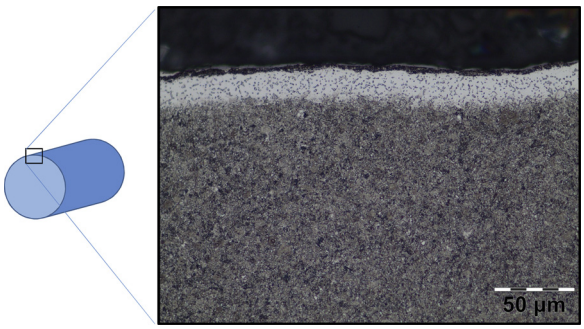

Fig. 1. Photomicrograph showing alpha case (white) layer on Ti6Al4V bar stock, annealed 2 hours at 760 °C in air and air cooled, revealed by partial immersion etching in ABF.

reflected light microscope (Olympus BX51RF, Japan) equipped with objectives ranging from 5× to 100×. The samples were evaluated in the as-polished, etched, and tint etched conditions to monitor changes in microstructure and/or composition resulting from the recycling process. Particles that displayed interesting features were indexed for subsequent evaluation by nanoindentation and SEM-EDS. Quantitative analyses of the void size and void concentration were performed on powder in the as-polished condition using image analysis software (Olympus cellSens Standard v. 1.18). Regarding void size, images of the voids were taken at 500× magnification and their caliper diameters were measured in 8 directions and averaged. Void concentration was measured at 100× magnification on random fields of view throughout the sample. Images were taken and analyzed using a custom script developed using commercial software (NIH ImageJ, Bethesda, MD, USA) to count the number of particles and voids in each image.

It is important to note that the voids were measured on a random cross-sectional plane, and their actual diameter in the particle cannot be directly measured. However if the voids are assumed to be spherical and are intersecting the evaluation plane at random points, the true size of the voids can be calculated based on the predicted area of the cross-section. Since it is equally probable to intersect the void at any point, the expected cross-sectional area becomes the average cross-sectional area as a function of height. For a spherical void sectioned randomly as depicted schematically in Fig. 2, the pore dimensions are described by

$$\bar{a} = \frac{1}{R-(-R)} \int_{-R}^{R} \pi(R^2 - y^2)dy \tag{1}$$

where ā is the average cross-sectional area, R is the true particle radius, and y is the distance of the intersecting plane from the center of the pore. The average cross-sectional area can be related to the measured radius r and the true radius R according to

$$\bar{a} = \sqrt{\frac{2}{3}}\pi R^2 = \pi r^2 \tag{2}$$

Then, the final relation between r and R, which is the same as the relation between the measured diameter d and the true diameter D is given by

$$R = \sqrt{\frac{3}{2}} r \rightarrow D = \sqrt{\frac{3}{2}} d \tag{3}$$

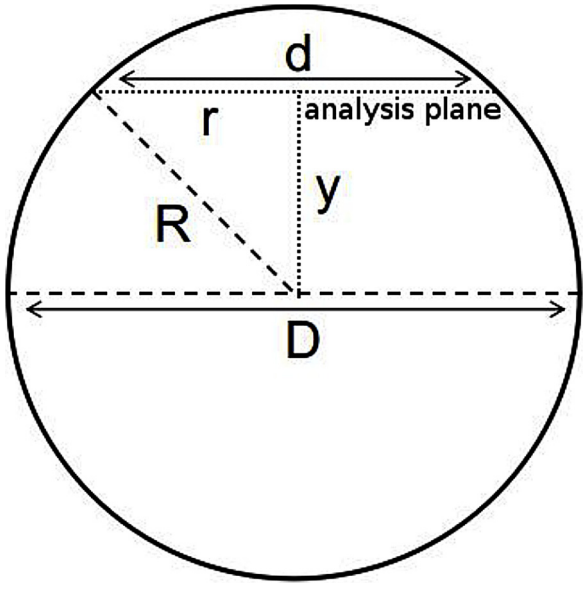

Fig. 2. Schematic diagram of dimensions used in calculating the true void diameter from the measured cross-section.

2.4.2. Nanoindentation

Hardness measurements were made on the cross-sectioned powder particles using a commercial nanoindenter system (Bruker Hysitron TriboIndenter 980, USA) with a Berkovich diamond indenter. A 2 mN indentation load was chosen such that the indents produced were small enough to be placed within a few microns from the edge of the particle, while deep enough to avoid complications from surface topography, contamination and indenter tip geometry. Under a 2 mN load, the indents had an edge length of approximately 1 μm and were approximately 100 nm deep. The testing conditions enabled indents to be placed as close as 2.5 μm from the edge of the particle, while abiding by the indent spacing requirements outlined in ASTM E 384-17 [27].

The powder sample mounts were secured to the nanoindenter stage using vacuum suction. For each particle investigated within a mount, a profilometer scan was taken and the desired indent locations were specified manually. The indent locations were chosen to obtain at least 3 indents close to the surface, a staggered array progressing inward to the core, and 5 indents near the center of the particle. The indents were examined using scanning probe microscopy to ensure that the indents were placed in the desired locations. These scans were also used to measure the radial distance from the indent center to the nearest edge.

The hardness and elastic modulus of the particles were evaluated using the standard Oliver and Pharr approach [28]. The nanoindentation hardness measurements were used to evaluate the presence of an alpha case layer and the potential for work hardening of the particles resulting from the PRS process. A hardness differential of 0.4 GPa between the surface and the core was used as the criteria for defining alpha case, which is based off an AMS material specification that defines surface contamination by a surface hardness more than 40 points higher than the subsurface hardness on the Knoop scale using a 200-gram load [29]. This requirement was adapted to nanoindentation methods to define alpha case.

The size of the indents needed to obtain reliable readings of the hardness limited how close they could be placed to the surface. Indents within 2.5 μm of the edge were considered invalid by the spacing requirements of ASTM E 384-17 [27]. Similarly, those with inconsistent shape and indents placed on surface irregularities were discarded as well. Consequently, indents between 2.5 μm and 5 μm of the surface were considered representative of the surface hardness. The core hardness was defined as the average of 5 indents placed roughly in the center of the particle.

2.4.3. SEM/EDS

An elemental analysis of the particles was performed using a commercial Scanning Electron Microscope (SEM; Phillips, Model XL30 Sirion FEI) equipped with an Energy-Dispersive x-ray Spectroscopy (EDS) detection system. The samples were carbon-coated prior to analysis to improve surface conductivity and prevent artifacts from sample charging. The EDS spectra were obtained with an accelerating voltage of 15 kV and a working distance of 5 mm. The beam spot size was adjusted to achieve a detector dead time of 30-50% for optimal signal collection. Surface-to-core line scans were taken to measure compositional gradients in the particles. The intensity of the oxygen signal was recorded as a function of distance from the particle edge.

3. Results

3.1. Optical Microscopy

3.1.1. Virgin Powder

A photomicrograph showing the structure of the virgin powder particles is shown in Fig. 3(a). The sample b1 (virgin) powder exhibited a microstructure consisting entirely of martensitic alpha prime (α'). This structure consists of fine, nearly indistinguishable acicular grains of alpha phase, and forms upon fast cooling from the beta phase. Tint etching with ABF highlighted the acicular structure but revealed no

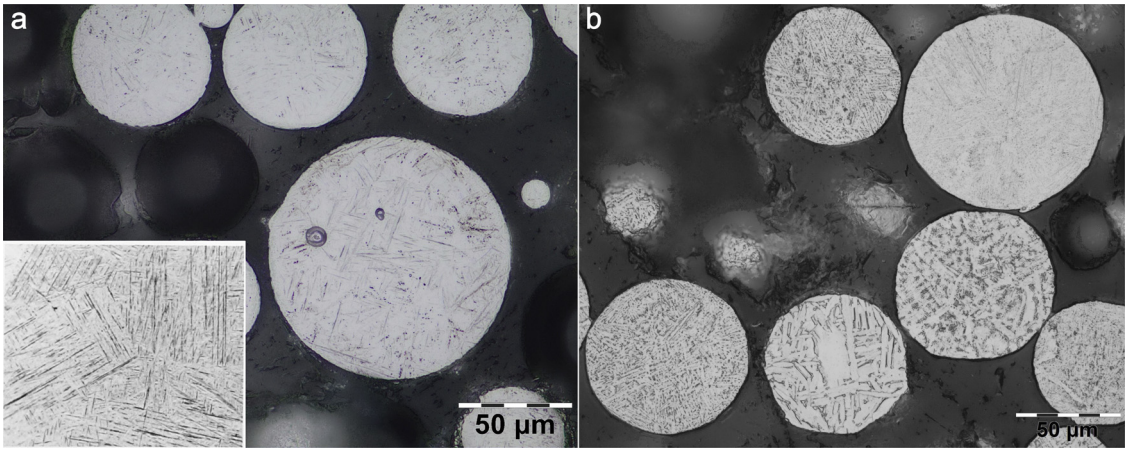

Fig. 3. Representative microstructure of particles at the beginning and end of the multiple build cycle. a) b1 (virgin powder) with reference. Insert shows Figure 2727 of ASM Metals Handbook Vol. 7, 8th Ed. showing a microstructure consisting entirely of alpha prime (martensite) formed in Ti-6Al-4 V forged at 1900 F, air cooled, annealed for 2 hours at 1300 F and quenched in water (Kroll's etch) [34]. b) b30 powder particles showing a range of microstructures.

alpha case layer on the particles, as expected. The particles were spherical, with small satellite particles occasionally visible along the margins of larger particles.

3.1.2. Reused Powder

A photomicrograph showing the structure of the reused powder particles of b30 is shown in Fig. 3(b). The reused powder showed a distribution of microstructures, ranging from near-virgin martensitic alpha to heavily coarsened alpha platelets with intergranular beta. Intermediate structures were visible in individual particles showing progressive levels of coarsening of the alpha grains, suggesting that individual powder particles experienced significantly different thermal histories. A view of the changes in microstructure over the reuse program is shown in Fig. 4. Specifically, a selection of particles from b7 and b14 are shown in Fig. 4(a-f). An view of the coarsest microstructure from b14 is shown in Fig. 4(f). The extent of observed coarsening and the range of the distribution of microstructures both increased with increasing reuse cycles. Specifically, the nearly virgin powder used in the early builds exhibited a few coarsened particles, whereas the powder in the later builds consisted almost entirely of heat-affected particles with relatively few particles still showing the virgin microstructure.

3.1.3. Alpha Case Standard

Photomicrographs of the heat treated powder (sample a1) under various etch conditions are shown in Fig. 5. Cross-sectioned particles are shown in the as-polished condition in 5(a), after being etched with Kroll's reagent in 5(b), and after etched with Kroll's and ABF in Fig. 5(c). The heat treated powder showed significant deterioration as a result of the thermally assisted oxidation. When removed from the furnace the powder was a matte orange-brown, visibly indicating the presence of a titanium oxide layer. In cross-section, a gray titanium oxide layer was visible on all the particles, coating them to a depth of approximately 10 µm. Surface cracks, chips, and crevasses were evident on the surfaces of the particles in the as-polished state as evident in all views in Fig. 5. The microstructure of the particles consisted of acicular alpha (transformed beta) that was not significantly coarsened from the martensitic virgin structure, owing to the relatively short duration of the heat treatment. The ABF tint etch revealed a thick white-etching layer (Fig. 5(c)), approximately 25 µm thick. Accurate total depth measurements of the white layer could not be measured from the cross-section, owing to the spherical geometry of the particles.

3.1.4. Accelerated PRS Powder

A photomicrograph of the particles subjected to the accelerated PRS treatment and after being etched with Kroll's and ABF is shown in Fig. 6. Many of the particles showed flattened faces and irregular, angular morphologies, a result of deformation caused by the impact forces experienced during the PRS treatment. In some instances, particles with large internal voids were observed to have fractured from the stress of the impacts, such as that shown in Fig. 7 (specifically Fig. 7c). The majority of the particles exhibited a fine martensitic structure when etched, similar to the microstructure of the virgin powder. A small percentage of the particles in the powder sample that underwent 30 hours of PRS cycling (t30) demonstrated coarsened microstructures and white etching layers when etched. These observations were attributed to errant particles trapped in the system from previous build and recovery cycles, and the particles showing these features were omitted in further analysis.

3.1.5. Voids

Voids were observed in all powder samples, and ranged in size from nearly indistinguishable to encompassing the entire particle volume. Examples of large voids observed in selected particles are shown in Fig. 7. The voids were consistent in shape, primarily round or oblong, except for the cases where the void encompassed the majority of the particle volume, resulting in structural instability and deformation.

The distribution in average measured void diameters is shown for selected powder samples over the powder reuse program in Fig. 8(a). No significant trend was observed in the void size as a function of build number for the reused powder. Image analysis measurements of the voids documented in the particles gave an overall average measured void diameter of 29 ± 12 µm, and a calculated true diameter of 35 ± 15 µm. The distribution in void occurrence is plotted for selected builds of the reused powder in Fig. 8(b). The frequency of void occurrence in the powder was determined to be about 1 void for every 100 particles, or a 1% void occurrence. This value was consistent across all powder samples over the history of the reuse process.

3.2. Nanoindentation

An example of the indentation array used for the hardness analysis of the titanium powder particles is shown in Fig. 9(a). Representative hardness profiles for selected particles of the alpha-case powder (a1p5) and the reused powder from build 30 (b30p19) are shown in Figs. 9(b) and 9(c), respectively. It is important to note that the data for these two particles is presented on different hardness ranges to accommodate the different peak hardness of the two conditions. There is a clear trend evident in both graphs reflecting the larger indentation hardness near the surface. The alpha-case particles (e.g. Fig. 9(b)) clearly exhibited

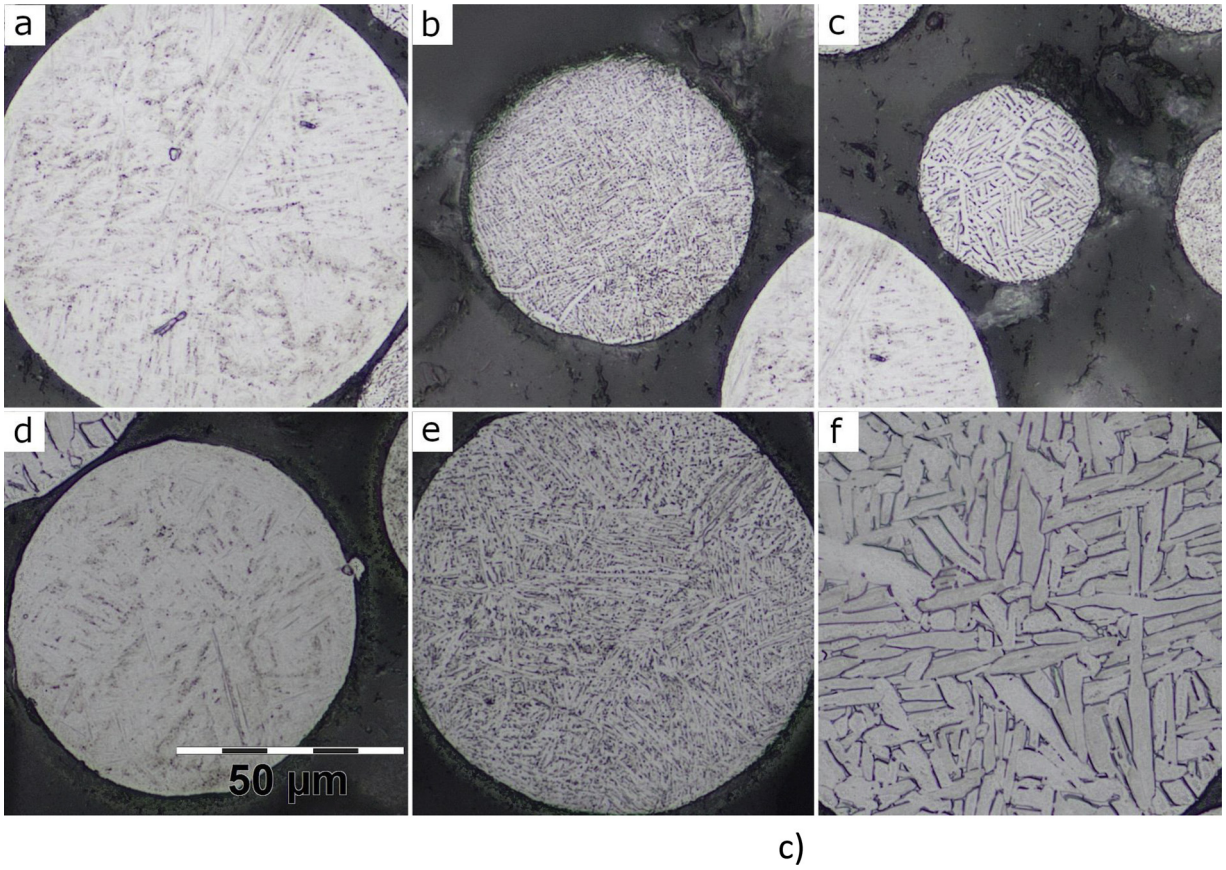

Fig. 4. Photomicrographs of particles from (a-c) b7 and (d-f) b14 representing the range of microstructures observed in those powder samples. (c) and (f) show photomicrographs of the coarsest microstructures observed in the respective powder samples. The scale for all the micrographs in (a-f) are the same.

the largest near-surface hardness.

For the alpha-case treated powder, three particles were selected for analysis based on the clarity of the white layer visible in the tint-etched condition. A photomicrograph of one of these particles is shown in Fig. 10(a). All three particles had significant surface hardening, with surface values being up to 15 GPa higher than the core. Similarly, a photomicrograph of one particle of the reused powder from b30 after the tint-etch process is presented in Fig. 10(b). A visible white layer is also evident. The average surface hardness for each particle was taken from the indents measured between 2.5 and 5 µm from the edge of the particle, which is well within the white layer. The measured values for the average core hardness and surface hardness of these particles is presented in Table 1, along with the hardness differentials. According to the measured hardness, the hardness differentials with regards to the

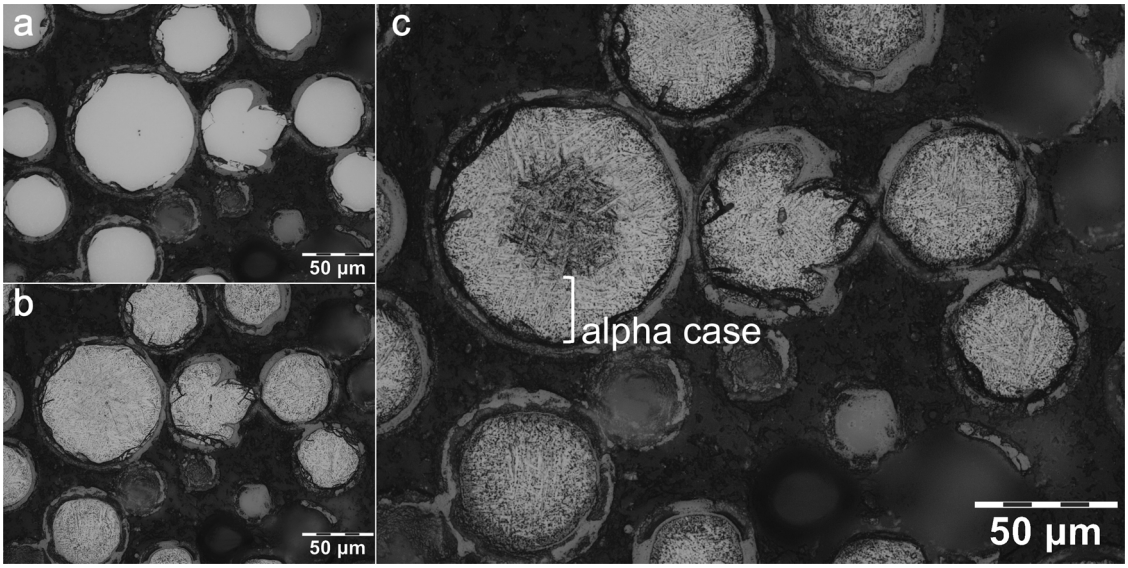

Fig. 5. Photomicrographs of the heat treated b1 powder in a) the as-polished condition, (b) etched with Kroll's reagent, and (c) etched with Kroll's and ABF. Note the light grey oxide layer surrounding each particle. The alpha case layer in indicated by the bracket.

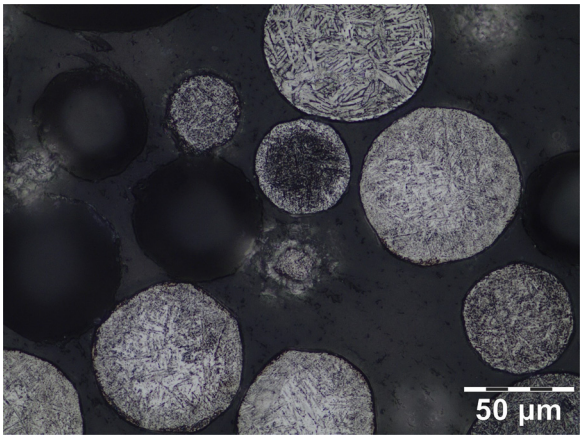

Fig. 6. Representative photomicrograph showing particles from the t30 powder sample (accelerated PRS powder) etched with Kroll's and ABF. Note the coarser microstructure on some of the particles, as well as the visible white layer on the center particle, suggesting these particles have experienced thermal cycling.

core for particle a1p4, a1p5, and a1p6 were 7.3, 5.4 and 6.6 GPa, respectively. All these values are > > 0.4 GPa hardness differential required for establishing the presence of an alpha-case. A visual comparison of the average surface hardness and average core hardness for the measured particles is plotted in Fig. 10(c).

Surface hardening in the reused powder was evident, although not to the extent of that in the alpha-case powder. The difference between the core and surface hardness appeared to increase with the extent of reuse. The average core hardness over the 30 builds was 5.0 ± 0.2 GPa, with no trend. However, the surface hardness increased from 4.7 ± 0.45 to 6.8 ± 0.4 GPa, which represents a significant increase over the 30 builds. Particle b1p2 from the b1 powder sample (virgin powder) showed a core hardness of 4.9 ± 0.3 GPa, with no change in hardness from the core to the edge. Particle b20 p14 showed a surface hardness of 5.6 ± 0.2 GPa, and a core hardness of 5.2 ± 0.3 GPa. This represents a hardness differential of 0.4 GPa, just at the alpha-case threshold. Particle b30p19 showed a surface hardness of 6.8 ± 0.4 GPa, and a core hardness of 4.9 ± 0.2 GPa. This represents a hardness differential of 1.9 GPa, sufficient to classify as alpha-case. The measured hardness values for particle b30p19 decreased to within 0.4 GPa of the average core hardness at approximately 20 µm from the surface.

The hardness distributions, as well as the average surface and core values were also evaluated for particles from the accelerated PRS study. These particles were selected based on optical micrographs for having microstructures similar to the virgin powder and evidence of mechanical deformation. A comparison of the average surface and core hardness for these particles is shown in Fig. 10(c); the measures of hardness and the hardness differentials are listed in Table 1. None of the particles from the accelerated PRS powder sample showed surface hardening in excess of 0.4 GPa from the average core hardness; average surface hardness values were within 0.4 GPa of the core values in all cases (Appendix A1 and A2).

3.3. SEM/EDS

EDS line scans from the surface of the alpha-case particles to the core showed significant changes in oxygen signal intensity, with the signal counts per second being up to three times higher at the surface as compared to the core (Fig. 11). The oxygen signal intensity drops rapidly towards the center of the particle, leveling off to values similar to those at the core by approximately 15 µm from the surface in the particles measured. Direct calculation of oxygen concentration cannot be determined by EDS due to limitations of the approach as well as complications due to energy peak overlap between oxygen and vanadium. Nevertheless, it is a useful approach for obtaining relative concentrations.

Although the presence of an alpha case layer in the reused powder is suggested from the tint etch and hardness measurements as shown in Figs. 9 and 10, there were no changes in oxygen signal intensity of the EDS scans detected between the surface and the core (Fig. 11). Similarly, the EDS analysis was also performed on the powder particles of the PRS study, with no discernible change in signal intensity from the surface to the core of these particles.

4. Discussion

The primary objective of this investigation was to evaluate the changes in properties of metal powder that occur over multiple build cycles in EBM with Grade 5 Ti6Al4V and to identify the primary contributing factors. According to results from the evaluation of microstructure, hardness profiles and composition, the findings suggest that oxygen diffusion occurs to the powder during the thermal cycles in EBM AM, which manifests as an alpha-case layer that extends from the surface inwards. The identification of alpha-case on the particles is a result of two different and independent measures, including the observation of oxygen contamination by the ABF tint etch, and identification of near-surface hardening through nanoindentation hardness testing. Surprisingly, substantial oxygen ingress in the feedstock was observed despite the use of vacuum in the EBM processing.

The ABF tint etch is a test often used to detect the presence of an alpha-case layer on titanium that has undergone heat treatments [30]. It is important to note, however, that other etch interactions can create lighter etching regions, and so the presence of a white surface layer is

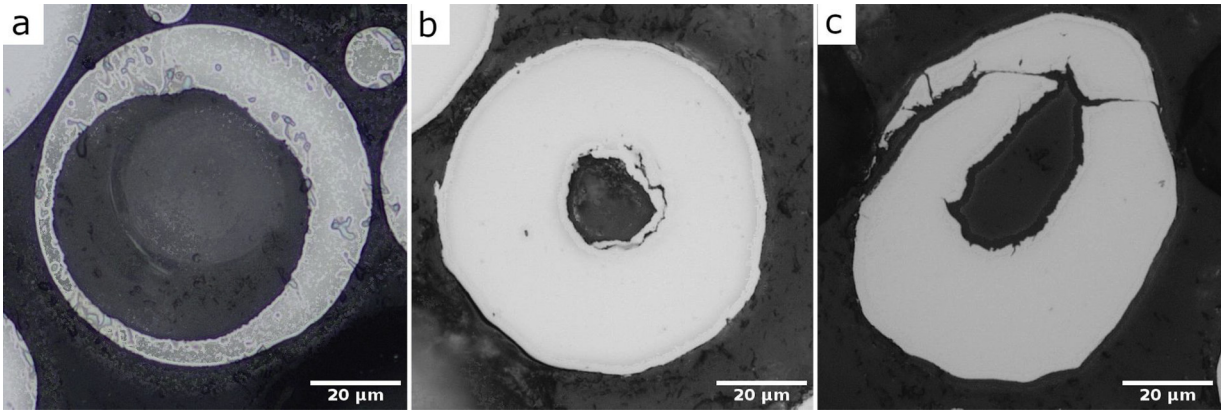

Fig. 7. Several examples of pores in powder particles as revealed by cross-sectioning. a) surface connected pore in b1 powder. b) internal pore in b30 powder. c) crushed pore in t30 powder.

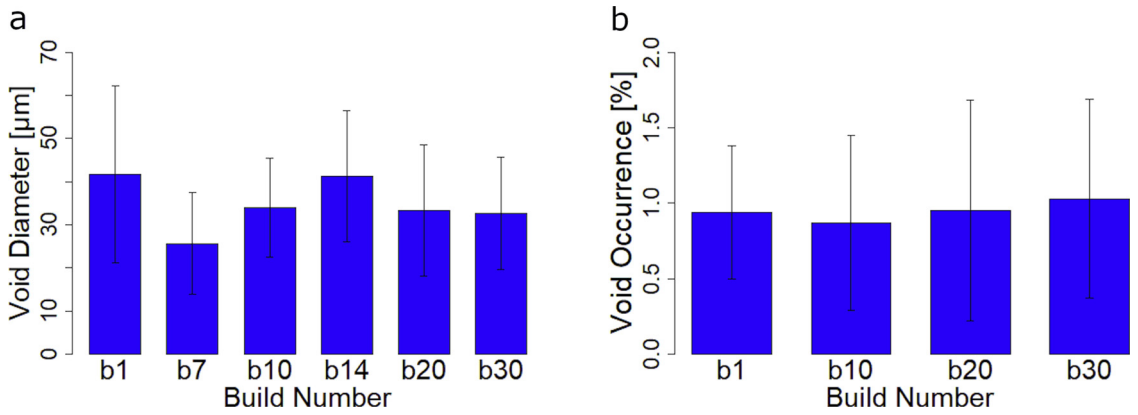

Fig. 8. Estimates for the (a) average void size and (b) void occurrence for selected powder samples.

not by itself sufficient evidence for confirmation of an alpha-case. As such, it is necessary to confirm the presence of the alpha-case through a secondary test, and most ideally a quantifiable measurement. For this reason, nanoindentation hardness testing was employed to examine hardness gradients from the particle surface that are related to either oxidation or another aspect of the processing.

One finding of importance is the relative agreement between the microstructure and hardness measurements, and their synergy. For instance, in all the particles with observed white layer and surface hardening, the subsurface hardness decreased below the alpha-case criteria limit at distances that were largely consistent with the measured depth of the white layer on those particles. That consistency is evident in the hardness profiles presented in Fig. 9(b) and (c) for the selected alpha-case and the reused powder particles, respectively. It not only provides supporting evidence that the white layer is indicative of alpha-case, but also suggests that the ABF tint offers an effective route for quantifying the depth of the alpha case. Nevertheless, the ABF tint etch alone is not sufficient to reliably claim alpha-case in all cases. Several particles were observed to exhibit a white layer but did not exhibit surface hardening. There were also particles that exhibited a prominent white layer and surface hardening, but the source of the hardening originated from sources other than oxygen. Admittedly, the estimated alpha-case depths may not represent true depths due to the random sectioning of the powder and potential deviation from the true-midplane. Depending on where the particle was sectioned, the skew of the surface relative to the polish plane can exaggerate the depth measurement, with greater exaggerations resulting from shallower cross-sections.

Although both the reused and alpha-case treated powders experienced similar levels of heat exposure (T≥ 700 °C), the reused powder underwent heating under vacuum while the a1 powder was exposed to air. The oxygen was much greater in the heat-treated powder (a1), enabling significantly more surface hardening as evident in Fig. 9. This was also evident optically by the presence of a more substantial and distinct oxide layer on the a1 powder particles. Thus, the lower extent of hardening in the heavily reused (b30) powder was expected due to the lower concentration of oxygen exposure. Furthermore, the individual particles of the reused powder experienced different thermal and chemical environments depending on their location within the build chamber, as well as differences in handling and their history in the mixing process. In fact, not all the b30 particles were expected to exhibit hardening. Hence, the findings presented here do not reflect the state of the reused powder globally, but rather present possible transformation routes that individual particles may take. Therefore, case hardening of the particles by oxygen diffusion is presented as a possibility in the powder, rather than a global certainty applicable to all particles. The particle mixing protocol and the proximity of the particles relative to the part boundaries in the build cycles are important contributions to the degradation process.

The absence of hardening in the accelerated PRS powder (t30) suggests that mechanical deformation does not cause significant surface hardening in Ti6Al4V powder particles. In fact, most of the t30 particles showed lower hardness near the surface than at the core. This could be a result of the limitations of the indentation approach near the surface

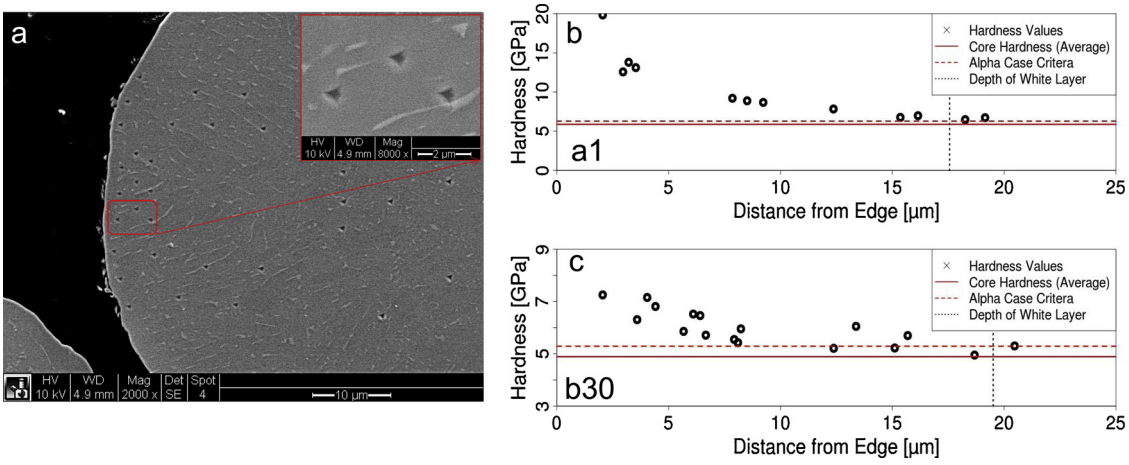

Fig. 9. Mapping of surface hardness. (a) SEM micrograph showing indents in a typical testing array. Inset shows details of indents (b) and (c) show the subsurface hardness profiles for selected particles from samples a1 and b30. The solid red line indicates the average core hardness for that particle, and the dashed red line indicates the 0.4 GPa difference used to define alpha-case. The vertical dotted black line indicates the depth of the white layer, as measured optically from the ABF tint.

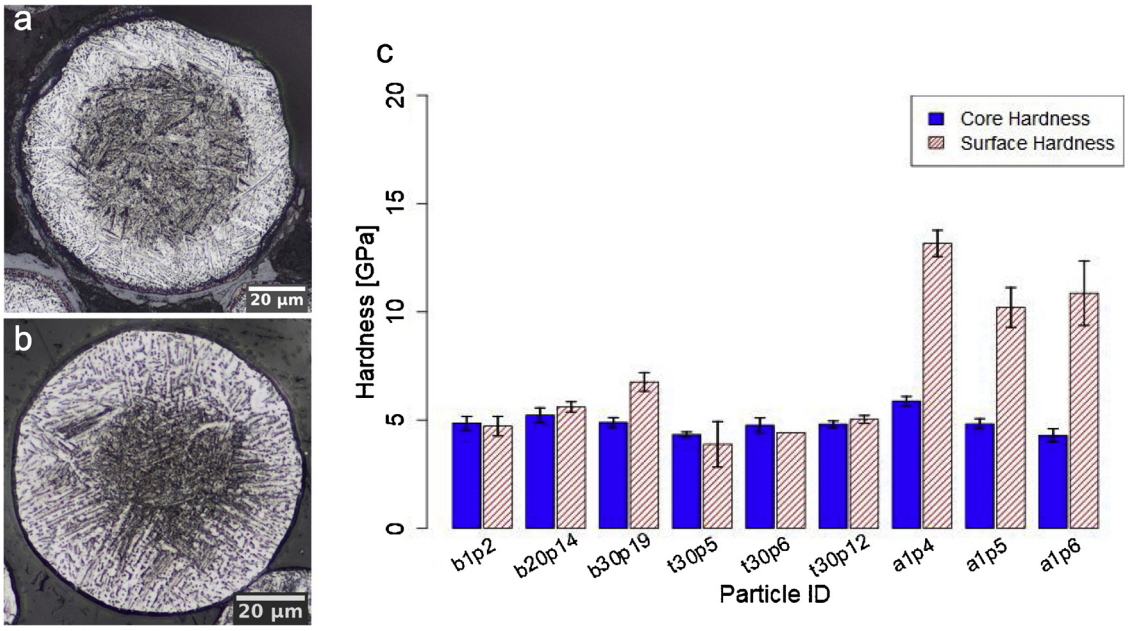

Fig. 10. Alpha case and particle properties. (a) and (b) show photomicrographs of particles a1p5 and b30p19, etched with Kroll's and ABF to reveal the alpha case. (c) shows the average surface and core hardness for each measured particle.

Table 1
Summary of average surface and core hardness for selected particles.

Sample	Average Surface Hardness (GPa)[1]	Average Core Hardness (GPa)[2]	Hardness Differential (GPa)
b1p2	4.72 ± 0.45	4.86 ± 0.31	−0.14 ± 0.55
b20p14	5.61 ± 0.24	5.23 ± 0.33	0.39 ± 0.40
b30p19	6.76 ± 0.43	4.89 ± 0.22	1.87 ± 0.48
t30p5	3.88 ± 1.05	4.33 ± 0.12	−0.45 ± 1.06
t30p6	4.41*	4.76 ± 0.34	−0.35*
t30p12	5.03 ± 0.18	4.81 ± 0.15	0.22 ± 0.24
a1p4	13.16 ± 0.61	5.88 ± 0.21	7.27 ± 0.65
a1p5	10.20 ± 0.92	4.82 ± 0.24	5.38 ± 0.95
a1p6	10.86 ± 1.49	4.29 ± 0.31	6.56 ± 1.53

[1] Average of indents from 2.5µm - 5µm of the surface.
[2] Average of 5 indents.
* No statistics are available.

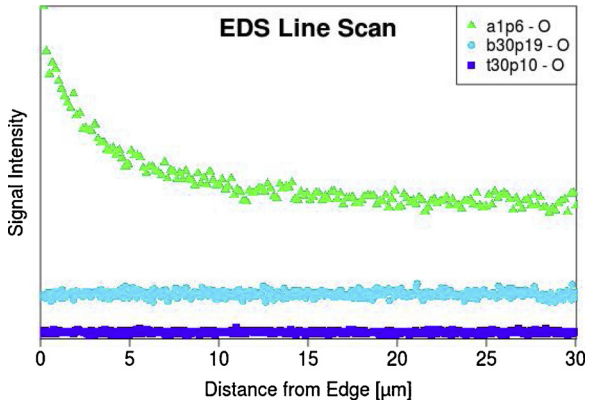

Fig. 11. Representative EDS line scan spectra showing oxygen Kα1 peak energy intensity as a function of distance from the particle edge for particles from samples a1, b30, and t30.

of cross-sectioned particles, causing the indenter to penetrate farther and giving the impression of softer material. It could also be a function of the limited depth of the hardened layer induced by deformation. The t30 powder was virgin powder introduced directly to the PRS. It did not undergo a heating process sufficient to allow significant oxygen diffusion into the metal. Since particles were selected for characterization based on the severity of their deformation, it is assumed that the examined particles represent worst-case scenarios. Therefore, since none of the particles showed signs of hardening, the work-hardening in particles with less-substantial signs of deformation would be equally minimal. Also noteworthy, the average void diameter and frequency of occurrence in the particles was not observed to change with reuse time. As such, crushing of particles with internal voids in the PRS is not a significant factor.

Although efforts were made to identify oxygen in the b30 powder via EDS methods, this approach proved unreliable in detecting the differences in oxygen concentration that had apparently occurred. Despite the tint etching and hardness measurements suggesting the presence of an alpha case layer on the b30 powder particles, it was not substantial enough to be observed from the oxygen signal intensity in the EDS line scans. Yet, this does not necessarily rule out the presence of an alpha case layer. Recent studies have suggested that a drastic change in mechanical properties occurs in titanium at an oxygen content of around 0.3 wt% [31]. Assuming that the oxygen concentration near the surface of the powder is at or around this level, it is close to the minimum detection limits for light elements on most EDS systems. This is further complicated due to the overlap between the oxygen K peak at 0.523 eV and the vanadium Kα peak at 0.511 eV [32]. Since vanadium is present in the particles at a nominal composition of 4 wt%, it is possible that the signal from the vanadium overwhelms small changes in the oxygen signal for the reused (b30) powder. This idea is supported by the EDS results of the heat-treated powder (a1) which leveled off to a consistent baseline before the hardness values passed below the alpha-case threshold. Apparently, the concentration of oxygen in the metal was sufficient to induce hardening but was below the detection limits by EDS.

Previous work by Tang et al. [5] attributed the increase in oxygen content of Ti6Al4V powder to oxygen pickup that occurs when it is exposed to air during the PRS, mixing, and sieving steps. While plausible, it is most likely that the main source of oxygen is actually water vapor in the air. When exposed, water molecules adsorb onto the surface of the powder particles. These molecules dissociate during the heating cycles in the EBM chamber, allowing the oxygen to penetrate the metal. This process has been previously shown to occur during gas

tungsten arc (GTA) welding of titanium alloys produced using powder metallurgy [33]. Another potential source of oxygen is the passive oxide layer that forms spontaneously on the surface of titanium metal when exposed to air [35]. Although only a few nanometers thick, progressive heating cycles and air exposure could cause the oxide layer to diffuse inward and reform periodically.

Despite the value of the findings in providing a fundamental understanding of the changes in powder particles with reuse in EBM with Ti6Al4V, there are limitations to this investigation that are important to consider. Primarily, the techniques used in this study only provide information on the individual particles measured. Thus drawing broader conclusions regarding the bulk properties of the powder are not recommended as they are a function of the individual powder handling procedures used, the manner in which additional powder is added incrementally in successive builds, etc. These are important issues that remain for future studies.

5. Conclusions

An experimental evaluation of Ti6Al4V metal powder particles was conducted over 30 build cycles of Electron Beam Melting (EBM) additive manufacturing (AM). For comparison, powder particles were also analyzed after an alpha-case heat treatment (control) and after accelerated mechanical processing by the powder recovery system (PRS). Based on morphological, microstructural, mechanical, and chemical analyses performed on cross-sectioned powder particles, the following conclusions are drawn:

i) The thermal cycling inherent to the EBM-PBF process causes coarsening of the particle microstructure. The extent of coarsening depends heavily on the specific thermal history of the individual particles, which depends on their location in the machine and with respect to the melt pool and part. Heavily reused powder is expected to exhibit a broad range of microstructures and thus a commensurately broad range of mechanical properties.
ii) The effect of oxygen diffusion in the powder is assumed to be cumulative with reuse times, with additional oxygen being introduced every time the powder is removed from the build chamber. Significant powder reuse can lead to the development of an oxygen rich case layer on a portion of the particles, which will depend on the volume of powder used in the build cycle and the particle proximity to heat.
iii) Surface hardening of the powder particles occurs during powder reuse. The hardening appears to result from contamination of the powder via external sources, with oxygen ingress representing one possible mechanism.
iv) Work hardening by mechanical deformation of the powder particles is not a significant factor in powder reuse. However, the mechanical deformation itself is an important factor in other aspects of powder reuse. Changes in powder morphology will undoubtedly affect the flowability and spreadability of the powder in the machine.
v) In EBM AM with Ti6Al4V and other powders that develop spontaneous passive oxide layers, it is essential to monitor/manage powder oxidation and its detrimental effects on the resultant built material. Concerted efforts should be made to develop systems that prevent powder exposure to oxygen sources, or to develop methods (chemical or physical) of removing the surface oxygen sources prior to each build.

Declaration of Competing Interest

The authors declare that they have no known competing financial interests or personal relationships that could have appeared to influence the work reported in this paper.

Acknowledgements

This work was partially accomplished using facilities funded by the Joint Center for Deployment and Research in Earth Abundant Materials (JCDREAM) in Washington State. The authors also gratefully acknowledge support for this investigation from The Boeing Company through the Boeing Advanced Research Center.

Appendix A

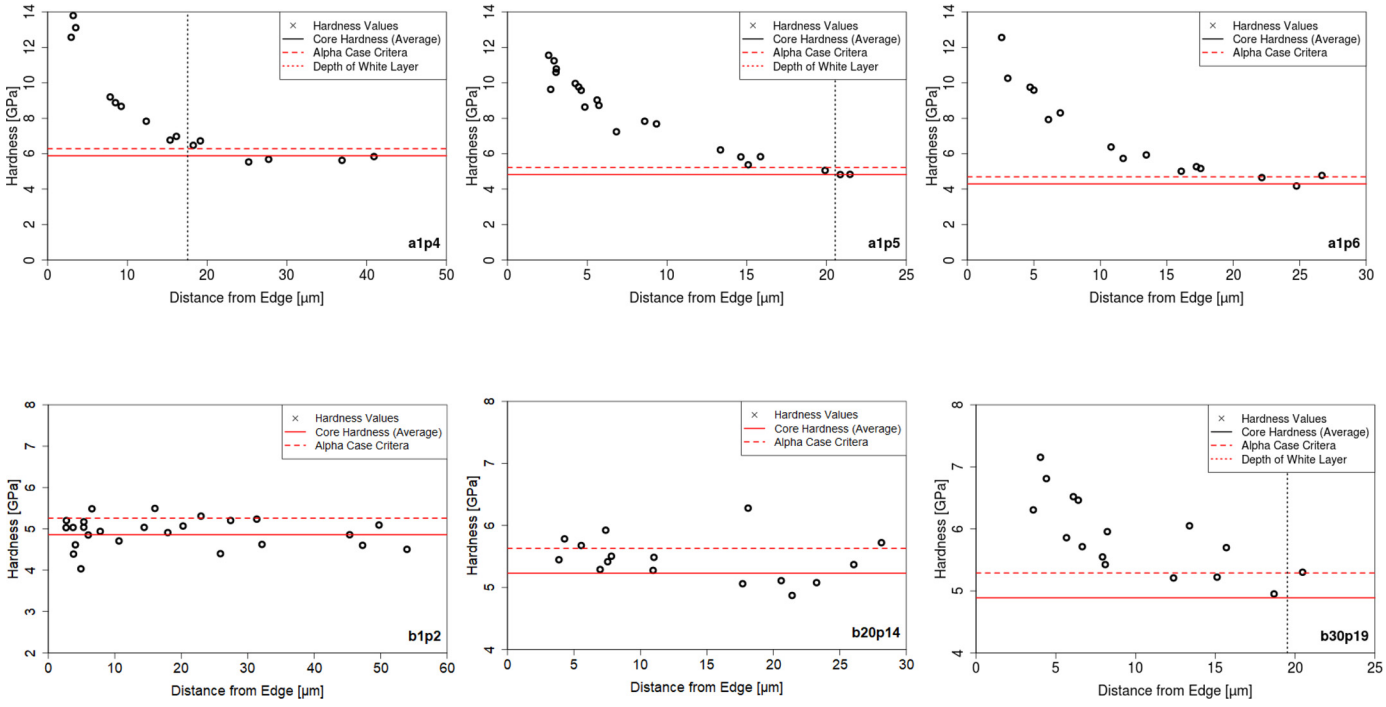

References

[1] T. DebRoy, H.L. Wei, J.S. Zuback, T. Mukherjee, J.W. Elmer, J.O. Milewski, W. Zhang, Additive manufacturing of metallic components – Process, structure and properties, Progress in Materials Science 92 (2018) 112–224, https://doi.org/10.1016/j.pmatsci.2017.10.001.

[2] D.L. Bourell, Perspectives on Additive Manufacturing, Annual Review of Materials Research 46 (1) (2016) 1–18, https://doi.org/10.1146/annurev-matsci-070115-031606.

[3] Y. Zhai, D.A. Lados, J.L. Lagoy, Additive Manufacturing: Making imagination the major Limitation, Jom 66 (5) (2014) 808–816, https://doi.org/10.1007/s11837-014-0886-2.

[4] Y. Sun, M. Aindow, R.J. Hebert, The effect of recycling on the oxygen distribution in Ti-6Al-4V powder for additive manufacturing, Materials at High Temperatures 35 (1–3) (2018) 217–224, https://doi.org/10.1080/09603409.2017.1389133.

[5] H.P. Tang, M. Qian, N. Liu, X.Z. Zhang, G.Y. Yang, J. Wang, Effect of Powder Reuse Times on Additive Manufacturing of Ti-6Al-4V by Selective Electron Beam Melting, Jom 67 (3) (2015) 555–563, https://doi.org/10.1007/s11837-015-1300-4.

[6] P. Nandwana, W.H. Peter, R.R. Dehoff, L.E. Lowe, M.M. Kirka, F. Medina, S.S. Babu, Recyclability Study on Inconel 718 and Ti-6Al-4V Powders for Use in Electron Beam Melting, Metallurgical and Materials Transactions B 47 (1) (2016) 754–762, https://doi.org/10.1007/s11663-015-0477-9.

[7] Renishaw, Investigating the effects of multiple re-use of Ti6Al4V powder in additive manufacturing, Renishaw (2016) 1–10.

[8] V. Petrovic, R. Niñerola, Powder recyclability in electron beam melting for aeronautical use, Aircraft Engineering and Aerospace Technology 87 (2) (2015) 147–155, https://doi.org/10.1108/AEAT-11-2013-0212.

[9] G. Lütjering, J. Williams, Titanium, Springer, Berlin, 2003.

[10] M.J. Jackson, W. Ahmed (eds), Titanium and Titanium Alloy Applications in Medicine, Surface Engineered Surgical Tools and Medical Devices, Springer, Boston, MA, 2007.

[11] X. Zhao, S. Li, M. Zhang, Y. Liu, T.B. Sercombe, S. Wang, Y. Hao, R. Yang, L.E. Murr, Comparison of the microstructures and mechanical properties of Ti-6Al-4V fabricated by selective laser melting and electron beam melting, Materials and Design 95 (2016) 21–31, https://doi.org/10.1016/j.matdes.2015.12.135.

[12] H.E. Boger, T.L. Gall, Metals handbook – desk edition, 3rd ed., ASM International, Materials Park, OH, 1986.

[13] T.M. Mower, M.J. Long, Mechanical behavior of additive manufactured, powder-bed laser-fused materials, Materials Science and Engineering A 651 (2016) 198–213, https://doi.org/10.1016/j.msea.2015.10.068.

[14] M. Svensson, U. Ackelid, Titanium Alloys Manufactured with Electron Beam Melting Mechanical and Chemical Properties, Materials & Processes for Medical Devices Conference (2009) 189–194 Retrieved from www.asminternational.org.

[15] J.J. Lewandowski, M. Seifi, Metal Additive Manufacturing: A Review of Mechanical Properties, Annual Review of Materials Research 46 (1) (2016) 151–186, https://doi.org/10.1146/annurev-matsci-070115-032024.

[16] J. Karlsson, M. Norell, U. Ackelid, H. Engqvist, J. Lausmaa, Surface oxidation behavior of Ti-6Al-4V manufactured by Electron Beam Melting (EBM®), Journal of Manufacturing Processes 17 (2015) 120–126, https://doi.org/10.1016/j.jmapro.2014.08.005.

[17] S. Zabler, Interstitial Oxygen diffusion hardening - A practical route for the surface protection of titanium, Materials Characterization 62 (12) (2011) 1205–1213, https://doi.org/10.1016/j.matchar.2011.10.012.

[18] J.R. Nicholls, M.J. Deakin, T. Rose, Surface Engineering of Titanium Alloys for High Temperature Applications, in: M. Winstone (Ed.), Titanium Alloys at Elevated Temperature: Structural Development and Service Behaviour, The Institute of Materials, London, 2001, pp. 187–218.

[19] T.A. Parthasarathy, W.J. Porter, S. Boone, R. John, P. Martin, Life prediction under tension of titanium alloys that develop an oxygenated brittle case during use, Scripta Materialia 65 (5) (2011) 420–423, https://doi.org/10.1016/j.scriptamat.2011.05.025.

[20] H. Conrad, Effect of interstitial solutes on the strength and ductility of titanium, Progress in Materials Science 26 (2–4) (1981) 123–403, https://doi.org/10.1016/0079-6425(81)90001-3.

[21] C. Wei, X. Ma, X. Yang, M. Zhou, C. Wang, Y. Zheng, W. Zhang, Z. Li, Microstructural and property evolution of Ti6Al4V powders with the number of usage in additive manufacturing by electron beam melting, Materials Letters 221 (2018) 111–114, https://doi.org/10.1016/j.matlet.2018.03.124.

[22] S. Ghods, E. Schultz, C. Wisdom, R. Schur, R. Pahuja, A. Montelione, D. Arola, M. Ramulu, Electron Beam Additive Manufacturing of Ti6Al4V: Evolution of Powder Morphology and Part Microstructure with Powder Reuse, Materialia. 9 (2020) 100631, , https://doi.org/10.1016/j.mtla.2020.100631.

[23] ASTM F2924-14, Standard Specification for Additive Manufacturing Titanium-6 Aluminum-4 Vanadium with Powder Bed Fusion, ASTM International, 2014, pp. 1–9, https://doi.org/10.1520/F2924-14.2 http://www.astm.org.

[24] V.V. Popov, A. Katz-Demyanetz, A. Garkun, M. Bamberger, The effect of powder recycling on the mechanical properties and microstructure of electron beam melted Ti-6Al-4 V specimens, Additive Manufacturing 22 (2018) 834–843, https://doi.org/10.1016/j.addma.2018.06.003.

[25] ASTM E407-07(2015)e1, Standard Practice for Microetching Metals and Alloys, ASTM International, West Conshohocken, PA, 2015, pp. 1–22 www.astm.org.

[26] F. Pitt, M. Ramulu, Influence of grain size and microstructure on oxidation rates in titanium alloy Ti-6Al-4V under superplastic forming conditions, Journal of Materials Engineering and Performance 13 (6) (2004) 727–734, https://doi.org/10.1361/10599490421394.

[27] ASTM E384-17, Standard Test Method for Microindentation Hardness of Materials, ASTM International, West Conshohocken, PA, 2017, pp. 1–40 www.astm.org.

[28] W.C. Oliver, G.M. Pharr, An improved technique for determining hardness and elastic modulus using load and displacement sensing indentation experiments, Journal Materials Research. 7 (1992) 1564–1583.

[29] SAE Aerospace Standard AMS 4911L, (2007).

[30] M.J. Donachie, Titanium a Technical Guide, 2nd ed., ASM International, 2000.

[31] H. Miura, Y. Itoh, T. Ueamtsu, K. Sato, The influence of density and oxygen content on the mechanical properties of injection molded Ti-6Al-4V alloys, Advances in Powder Metallurgy and Particulate Materials-2019 vol. 4, MPIF, Princeton, NJ, 2010, pp. 46–53.

[32] D.E. Newbury, N.W.M. Ritchie, Performing elemental microanalysis with high accuracy and high precision by scanning electron microscopy/silicon drift detector energy-dispersive X-ray spectrometry (SEM/SDD-EDS), Journal of Materials Science 50 (2) (2014) 493–518, https://doi.org/10.1007/s10853-014-8685-2.

[33] T.R. Muth, Y. Yamamoto, D.A. Frederick, C.I. Contescu, W. Chen, Y.C. Lim, W.H. Peter, Z. Feng, Causal factors of weld porosity in gas tungsten arc welding of powder-metallurgy-produced titanium alloys, Jom 65 (5) (2013) 643–651, https://doi.org/10.1007/s11837-013-0592-5.

[34] American Society for Metals, Metals Handbook, in: Cleveland (Ed.), The Society, 8th ed., 1961.

[35] Ruslan Shvab, Eduard Hryha, Lars Nyborg, Surface chemistry of the titanium powder studied by XPS using internal standard reference, Powder Metallurgy 60 (1) (2017) 42–48, https://doi.org/10.1080/00325899.2016.1271092 Surface.